Gravity wave characteristics in the middle atmosphere derived from the Empirical Mode Decomposition method

Xun Zhu,[1,2] Zheng Shen,[2] Stephen D. Eckermann,[3,4]
Michael Bittner,[5] Isamu Hirota,[6] and Jeng-Hwa Yee[1]

Abstract. The recently developed Empirical Mode Decomposition (EMD) method is applied to analyzing gravity wave characteristics in the middle atmosphere. By establishing a close connection between the fundamental Intrinsic Mode Functions (IMFs) derived from the EMD method and WKB solutions of a dispersive-dissipative wave equation, we show that the EMD method can provide useful insights into physical processes in the middle atmosphere where dispersive-dissipative wave phenomena are dominant. A local power spectrum function P is introduced which provides a quantitative description of the spectrum at any particular location within a data series. The sharp localization of P in space and wavenumber leads to an identification of unphysical small scale oscillations by falling spheres embedded in the wind profiles above 60 km. Further analyses of the horizontal wind profiles derived from the Dynamics Adapted Network for the Atmosphere (DYANA) campaign suggest that for horizontal wind fluctuations with vertical wavenumber $m \leq 3$ km^{-1} (or vertical wavelength $L_z \geq 2$ km) the previously observed m^{-3} Fourier spectra could be produced by a linear wave packet whose characteristic vertical wavenumber decreases with altitude. For small vertical scale disturbances with $m > 3$ km^{-1} ($L_z < 2$ km) a near -3 slope in the marginal distribution exists locally in the middle atmosphere with a great degree of universality, suggesting that nonlinear energy cascade processes may dominate the spectral formation in this wavenumber range.

1. Introduction

In recent years, internal gravity waves have been extensively studied in the middle atmosphere for two major reasons. First, there are strong reasons to believe that gravity waves are the primary source of the observed mesoscale fluctuations in the middle atmosphere. Second, the deposition of the momentum and energy carried by the gravity waves plays a central role in establishing the large-scale circulation and structure of the middle atmosphere. Many observations have suggested a simple form of m^{-p} with $p \sim 3$ for the Fourier vertical wavenumber m power spectra of horizontal velocity and relative temperature fluctuations in the atmosphere at large m. Many different theories have been developed to explain the nearly m^{-3} spectra observed at large m [e.g., *Dewan and Good*, 1986; *Smith et al.*, 1987; *Weinstock*, 1990; *Hines*, 1991; *Gardner*, 1994; *Zhu*, 1994], without certainty of which theory, if any, is valid [*Gardner*, 1996].

Clearly, to better parameterize the drag and eddy diffusion induced by gravity waves in the middle atmosphere, it is im-

portant to identify the major physical mechanisms driving the observed m^{-3} power spectra. Some of the difficulties involved in identifying the dominant physical mechanism could be associated with the strong inhomogeneity of the atmosphere. Vertically propagating gravity waves subject to atmospheric stratification and wind shear have nonstationary wave amplitudes [e.g., *Eckermann*, 1990; *Hines*, 1991]. On the other hand, traditional Fourier spectral analysis decomposes a series of data into a linear combination of infinite harmonic functions which have constant amplitudes over the whole data series. Thus Fourier methods are not ideal for studying nonstationary gravity wave process. There are many useful tools in data analysis that provide both spatial and wavenumber information to study nonstationary processes [e.g., *Daubechies*, 1992; *Cohen*, 1995]. For example, wavelet analysis has been applied to studying spatial and temporal variations in gravity wave activity measured in the lower stratosphere [*Sato and Yamada*, 1994; *Shimomai et al.*, 1996; *Bacmeister et al.*, 1996, 1997].

Recently, a new technique called Empirical Mode Decomposition (EMD) has been developed to study the nonlinear and nonstationary properties of time series [*Huang et al.*, 1997]. The EMD method has been shown to be superior in some circumstances to existing data analysis tools such as the wavelet analysis [*Huang et al.*, 1997]. In this paper, the EMD method is used to assess the predictions of current linear and nonlinear gravity wave theories of the observed m^{-3} power spectra in the middle atmosphere.

In the next section we first review the EMD method and show that the fundamental Intrinsic Mode Functions (IMFs) derived from the EMD method are closely related to the WKB solutions of an equation describing dispersive-dissipative wave phenomena. In section 3, a two-dimensional distribution function called local power spectrum denoted by $P(z_k, m_\ell)$ is

Report Documentation Page	Form Approved OMB No. 0704-0188

Public reporting burden for the collection of information is estimated to average 1 hour per response, including the time for reviewing instructions, searching existing data sources, gathering and maintaining the data needed, and completing and reviewing the collection of information. Send comments regarding this burden estimate or any other aspect of this collection of information, including suggestions for reducing this burden, to Washington Headquarters Services, Directorate for Information Operations and Reports, 1215 Jefferson Davis Highway, Suite 1204, Arlington VA 22202-4302. Respondents should be aware that notwithstanding any other provision of law, no person shall be subject to a penalty for failing to comply with a collection of information if it does not display a currently valid OMB control number.

1. REPORT DATE **1997**	2. REPORT TYPE	3. DATES COVERED **00-00-1997 to 00-00-1997**
4. TITLE AND SUBTITLE **Gravity wave characteristics in the middle atmosphere derived from the Empirical Mode Decomposition method**		5a. CONTRACT NUMBER
		5b. GRANT NUMBER
		5c. PROGRAM ELEMENT NUMBER
6. AUTHOR(S)		5d. PROJECT NUMBER
		5e. TASK NUMBER
		5f. WORK UNIT NUMBER
7. PERFORMING ORGANIZATION NAME(S) AND ADDRESS(ES) **Naval Research Laboratory,E.O. Hulburt Center for Space Research,Washington,DC,20375**		8. PERFORMING ORGANIZATION REPORT NUMBER
9. SPONSORING/MONITORING AGENCY NAME(S) AND ADDRESS(ES)		10. SPONSOR/MONITOR'S ACRONYM(S)
		11. SPONSOR/MONITOR'S REPORT NUMBER(S)

12. DISTRIBUTION/AVAILABILITY STATEMENT
Approved for public release; distribution unlimited

13. SUPPLEMENTARY NOTES

14. ABSTRACT
see report

15. SUBJECT TERMS

16. SECURITY CLASSIFICATION OF:			17. LIMITATION OF ABSTRACT	18. NUMBER OF PAGES	19a. NAME OF RESPONSIBLE PERSON
a. REPORT **unclassified**	b. ABSTRACT **unclassified**	c. THIS PAGE **unclassified**	**Same as Report (SAR)**	**17**	

Standard Form 298 (Rev. 8-98)
Prescribed by ANSI Std Z39-18

introduced to provide a quantitative description of space-wavenumber $(z\text{-}m)$ localization, where z and m are the altitude and vertical wavenumber, respectively. Similarities and differences between the marginal distribution of $P(z_k, m_\ell)$ and the Fourier spectrum of a data series are clarified. Section 4 discusses the local power spectrum calculated from the observations. Section 5 identifies one IMF as a characteristic gravity wave component in the middle atmosphere. Finally, in section 6 we summarize our EMD-derived results for gravity waves.

2. Local Wavenumber and Empirical Mode Decomposition Method

Given a digital signal or a data series of a quantity u expressed as a real function of a time or space variable ξ, $u(\xi)$, one can construct a complex signal, $U(\xi)$, by adding an imaginary function $i\hat{u}(\xi)$ to the original signal

$$U(\xi) = u(\xi) + i\hat{u}(\xi) = U_0(\xi) \exp [i\phi(\xi)], \quad (1)$$

where

$$U_0(\xi) = [u^2(\xi) + \hat{u}^2(\xi)]^{1/2}, \quad (2)$$

and

$$\phi(\xi) = \arctan \frac{\hat{u}(\xi)}{u(\xi)} \quad (3)$$

are the amplitude and the phase of the signal, respectively [Cohen, 1995]. When the independent variable ξ represents space (time), a local wavenumber (instantaneous frequency) can be derived from (3)

$$\phi'(\xi) = \frac{u(\xi)\hat{u}'(\xi) - \hat{u}(\xi)u'(\xi)}{U_0^2(\xi)}, \quad (4)$$

where the prime denotes the derivative (i.e., $\phi' = d\phi/d\xi$). In this paper, we are mostly interested in wind fluctuations as a function of space. Therefore a local wavenumber $\kappa(\xi) = \phi'(\xi)$ for the complex signal $u(\xi)$ is provided by (4). When expressed in terms of amplitude and wavenumber, the complex signal (1) can also be written as

$$U(\xi) = U_0(\xi) \exp \left[i \int_0^\xi \kappa(\tau) \, d\tau \right]. \quad (5)$$

An optimal choice for the imaginary function $i\hat{u}(\xi)$ that gives an unambiguous local wavenumber is the Hilbert transform of the signal $u(\xi)$ [Cohen, 1995], defined as

$$H[u(\xi)] = \hat{u}(\xi) = \frac{1}{\pi} \int_{-\infty}^{\infty} \frac{u(\tau) \, d\tau}{\xi - \tau}, \quad (6)$$

where the integral is a Cauchy principle value and H is the Hilbert transform operator. The complex signal thus defined by (1) and (6) is called an analytic signal belonging to $u(\xi)$ [e.g., Bracewell, 1986; Cohen, 1995]. Likewise, $U_0(\xi)$ and $\phi'(\xi)$ are the amplitude and wavenumber of the analytic signal belonging to the original signal $u(\xi)$. Cohen [1995] shows under certain restricted conditions that for the analytic signal defined by (1) and (5) there is no overlap between the wavenumber spectra of $U_0(\xi)$ and $\exp [i\phi(\xi)]$. In other words, the process of constructing an analytic signal $U(\xi)$ from a real signal $u(\xi)$

is to put the slowly varying content of $u(\xi)$ into the amplitude $U_0(\xi)$ and to put the fast varying content into $\exp [i\phi(\xi)]$. Mathematically, as long as the Hilbert transform (6) exists, one can always find an amplitude $U_0(\xi)$ and a wavenumber $\kappa(\xi)$ from (2) and (4) for any real function $u(\xi)$. However, the derived $U_0(\xi)$ and $\kappa(\xi)$ based on such a direct procedure are not always physically meaningful. The difficulties are summarized by Cohen [1995] into five paradoxes about the properties of the local wavenumber. It turns out that the major difficulties in finding physically meaningful local wavenumber and amplitude for a real signal depend on how well separated the spectra of $U_0(\xi)$ and $\exp [i\phi(\xi)]$ are. The recently developed Empirical Mode Decomposition (EMD) method helps to resolve this key issue by decomposing a real signal $u(\xi)$ into a set of different components so that the $U_0(\xi)$ spectrum and $\exp [i\phi(\xi)]$ spectrum for each component are separated [Huang et al., 1997]. In the following, we briefly review and extend the basic ideas of EMD method.

It is noted that (5) often appears as a WKB solution of a wave packet to a wave equation that includes both dispersive and dissipative phenomena [e.g., Bender and Orszag, 1978]

$$\frac{d^2U}{d\xi^2} + n^2U = 0, \quad (7)$$

where the refractive index n describes wave-medium interaction and it can be complex. We define the complex refraction index by $n^2 = n_r^2 + in_i^2$. In general, the dispersive phenomenon is described by a spatial variation of n_r^2, whereas the dissipation effects are formulated by a nonzero n_i^2 term. When expressed in terms of (5), the WKB solutions of (7) are given by [e.g., Einaudi and Hines, 1970; Wait, 1981]

$$U_0(\xi) = \frac{C_{1,2}}{\sqrt{n_r(\xi)}} \exp \left[\pm \int^\xi \frac{n_i(\tau)^2}{n_r(\tau)} \, d\tau \right], \quad (8a)$$

$$\kappa(\xi) = n_r(\xi), \quad (8b)$$

where $C_{1,2}$ are integration constants for each of two wave packets propagating in opposite directions. The posterior condition that (5) and (8) are valid solutions of (7) is a slowly varying envelope of the wave packet for each wave component [e.g., Einaudi and Hines, 1970; Wait, 1981]

$$\left| \frac{1}{U_0} \frac{d^2U_0}{d\xi^2} \right|^{1/2} \ll \kappa = n_r. \quad (9)$$

If we define the left-hand side of (9) as a local characteristic inverse scale $K(\xi)$ of the envelope for the wave packet, then the validity condition of the WKB approximation can be rewritten as

$$\left| \frac{1}{U_0} \frac{d^2U_0}{d\xi^2} \right|^{1/2} \equiv K(\xi) \ll \kappa(\xi). \quad (10)$$

Therefore, in order that an analytic signal (5) represents a physically meaningful wave packet with an envelope $U_0(\xi)$ and a local wavenumber $\kappa(\xi)$, the local characteristic inverse scale of $U_0(\xi)$ should be well separated from the local wavenumber $\kappa(\xi)$ of the analytic signal. Condition (10) can be considered as an acceptable working criterion for sufficient separation between the $U_0(\xi)$ spectrum and $\exp [i\phi(\xi)]$ spectrum.

Condition (10) requires the spectral separation at local points of ξ. We can also propose the following global condition
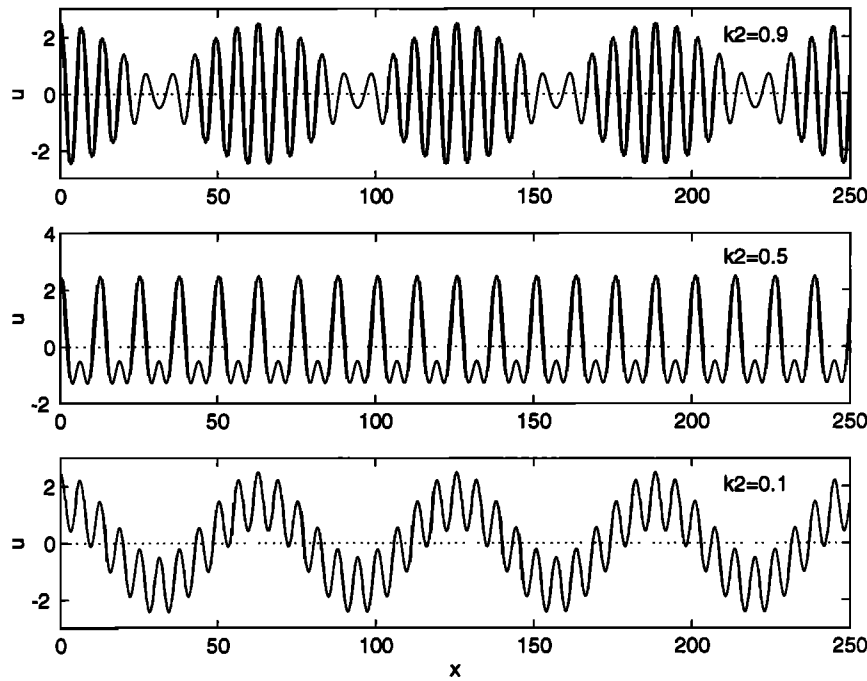
Figure 1. Real signals of a superposition of two sinusoidal waves defined by (12) with $a_1 = 1$, $a_2 = 1.5$, and $k_1 = 1$: (top) $k_2 = 0.9$; (middle) $k_2 = 0.5$; and (bottom) $k_2 = 0.1$. The dotted lines denote 0.

for spectral separation by defining a wave energy-weighted index of separation χ

$$\chi \equiv \frac{\left| \dfrac{1}{L} \int_L \dfrac{d^2 U_0}{d\xi^2} U_0^3 \, d\xi \right|^{1/2}}{\left| \dfrac{1}{L} \int_L \kappa U_0^2 \, d\xi \right|} \ll 1, \qquad (11)$$

where L is the total length of a digital signal.

To illustrate the above conjecture more clearly and to see how the EMD method generally results in a clear separation between $K(\xi)$ and $\kappa(\xi)$ for each empirical mode, we now consider a well known example of a superposition of two sinusoidal signals with different wavenumbers

$$u(x) = a_1 \cos (k_1 x) + a_2 \cos (k_2 x). \qquad (12)$$

Without loss of generality we first fix the values of $a_1 = 1$, $a_2 = 1.5$, and $k_1 = 1$. Letting k_2 change between 0 and 1, we then examine $U_0(x)$, $K(x)$, and $\kappa(x)$. In Figure 1 we show three plots of $u(x)$ with decreasing values of k_2 from 0.9 to 0.1. Although the high frequency oscillatory feature $k_1 = 1$ exists in all three signals, Figure 1 shows that the basic character of the large-scale variations is totally different. When $k_2 \approx k_1$, the signal resembles a wave packet with slowly varying envelope, while when $k_2 \ll k_1$, the signal represents small scale disturbances riding on a large-scale background field. The analytic signal belonging to (12) can be derived easily based on the basic formula $H[\cos (kx)] = \sin (kx)$ [e.g., Bracewell, 1986; Karl, 1989]. The local amplitude $U_0(x)$ and the local wavenumbers $\kappa(x)$ and $K(x)$ defined by (2), (4), and (10) for the analytic signal are [Cohen, 1995]

$$U_0(x) = [(a_1 - a_2)^2 + 4a_1 a_2 \cos^2 (k_d x)]^{1/2}, \qquad (13a)$$

$$\kappa(x) = k_m - k_d \frac{a_1^2 - a_2^2}{U_0(x)^2}, \qquad (13b)$$

$$K(x) = \frac{|k_d|}{U_0(x)^2}$$

$$\cdot |4a_1 a_2[(a_1 - a_2)^2 \cos (2k_d x) + 4a_1 a_2 \cos^4 (k_d x)]|^{1/2}, \qquad (13c)$$

where k_m and k_d denote the average and the difference of the two basic wavenumbers

$$k_d = \frac{k_1 - k_2}{2}, \qquad k_m = \frac{k_1 + k_2}{2}. \qquad (14)$$

Figure 2 shows the plots of $U_0(x)$, $\kappa(x)$, and $K(x)$ for the three cases. The indices of separation χ for the three cases are 0.061, 0.432, and 1.35, respectively. We may immediately conclude the following: (1) when the conditions (10) and (11) are well satisfied as in the case $k_2 = 0.9$, the local wavenumber $\kappa(x)$ approximately equals the fast varying basic wavenumber k_1 in the original real signal and varies slightly with x; (2) when (10) and (11) are not satisfied, the local wavenumber $\kappa(x)$ departs significantly from the basic wavenumber k_1 or becomes negative. To see how the index of separation χ also varies with the amplitudes a_1 and a_2 of basic sinusoidal waves, we show in Figure 3 the plot of Log_{10} (χ) as a function of two parameters $\delta = a_2/a_1$ and $\varepsilon = k_d/k_m$, where

$$\chi = \frac{\sqrt{6}|\varepsilon|}{|\delta^{-1} + \delta + \varepsilon(\delta^{-1} - \delta)|}. \qquad (15)$$

Figure 3 shows that the index of separation χ will be small when the amplitudes of the two basic wave components differ significantly ($a_1 \ll a_2$ or $a_2 \ll a_1$) even if their wavenumbers differ significantly ($\varepsilon \sim 1$). Clearly, the local wavenumber of the analytic signal under such a circumstance is approxi-
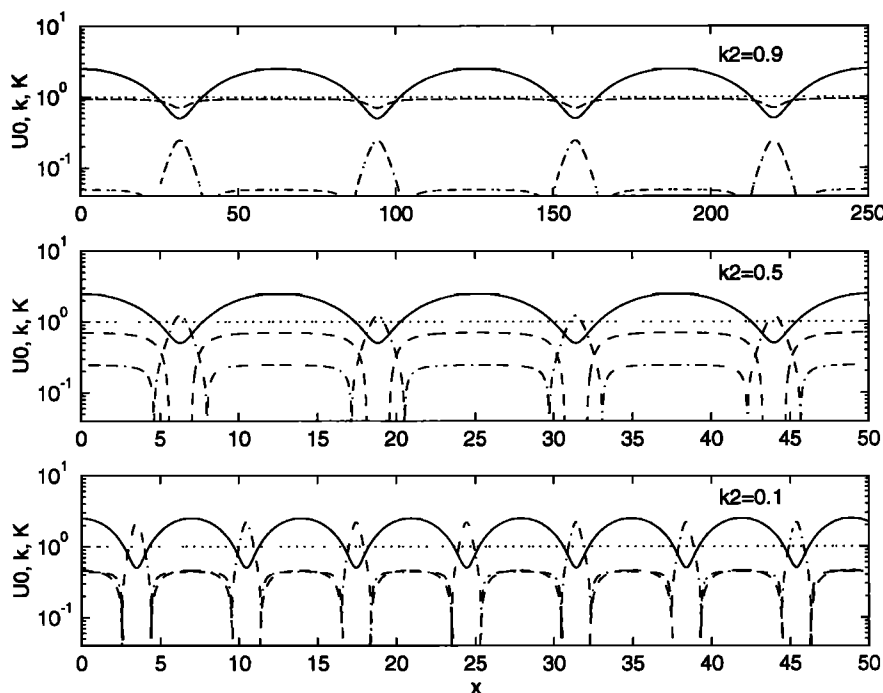
Figure 2. The amplitude U_0 (solid lines) and local wave numbers $\kappa(x)$ (dashed lines) and $K(x)$ (dash-dotted lines) of the analytic signals belonging to the real signals of Figure 1. The dotted lines denote 1.

mately equal to the basic wavenumber that has a dominant amplitude. A signal with $a_1 \ll a_2$ or $a_2 \ll a_1$ corresponds to a major wave component with a small riding wave or with a small asymmetric distortion, respectively.

Returning to Figure 1 where $a_1 \sim a_2$, we find that the fast varying mode corresponding to $k_1 \sim 1$ exists visibly in all the signals no matter what the local wavenumber $\kappa(x)$ is. The central idea of the EMD method is to separate locally the fast varying mode from the background slowly varying mode by a recursive sifting process [*Huang et al.*, 1997]. The sifting process extracts a signal by subtracting the mean of two envelopes which are formed by smoothly interconnecting local maxima and local minima in the data series, respectively. Each such signal is called an Intrinsic Mode Function (IMF). Each IMF is subtracted from the data series, and the process is repeated until all the variability in the data series is decomposed into a number of these IMFs. Generally speaking, each IMF has the form of a wave packet which satisfies the validity condition (10). For a more precise definition of the IMF, detailed development and implementation of the EMD method, Hilbert spectrum analysis, and their various applications in analyzing nonlinear and nonstationary time series, readers are referred to the work of *Huang et al.* [1997]. When applying the EMD method to the present example (Figure 4), we recover the two basic sinusoidal components as their IMFs for the second and third cases where the condition (10) and (11) are not well satisfied. However, the IMF for the first case is the signal itself that has a slight local wavenumber modulation and a significant amplitude modulation in space.

Since the derived IMF for the first case is a wave packet with an amplitude and wavenumber modulation, then the EMD technique may be particularly useful in analyzing and interpreting dispersive-dissipative wave-related data. We know from the construction that the signal in case 1 corresponds to a superposition of two sinusoidal waves with distinct wavenum-

bers and constant amplitudes. On the other hand, the wave packet IMF derived from the EMD method and indicated by (5) and (13) suggests that there exists only one mode in the original signal. Although the two expressions are identical mathematically, they may have different physical origins. For example, the signal in the first case can be produced either by two wavemakers that have distinct frequencies and constant amplitudes or by one wavemaker with a fixed frequency and a
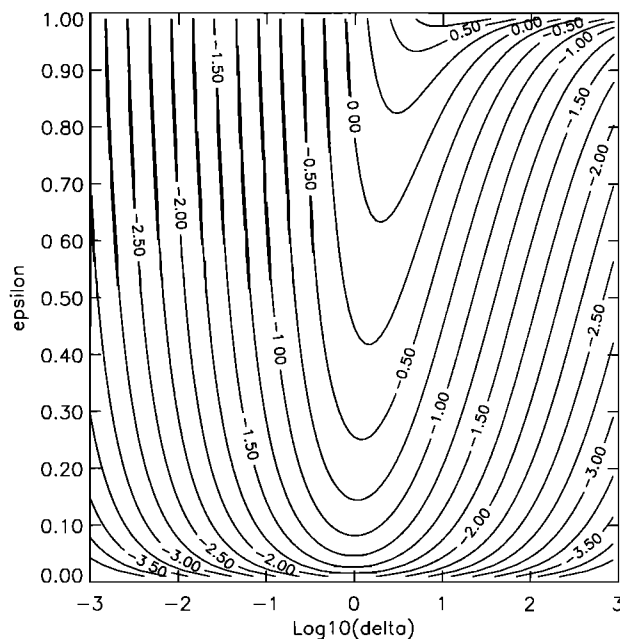

Figure 3. Logarithm of index of separation, $\mathrm{Log}_{10}(\chi)$, as a function of $\mathrm{Log}_{10}(\delta)$ and ε.
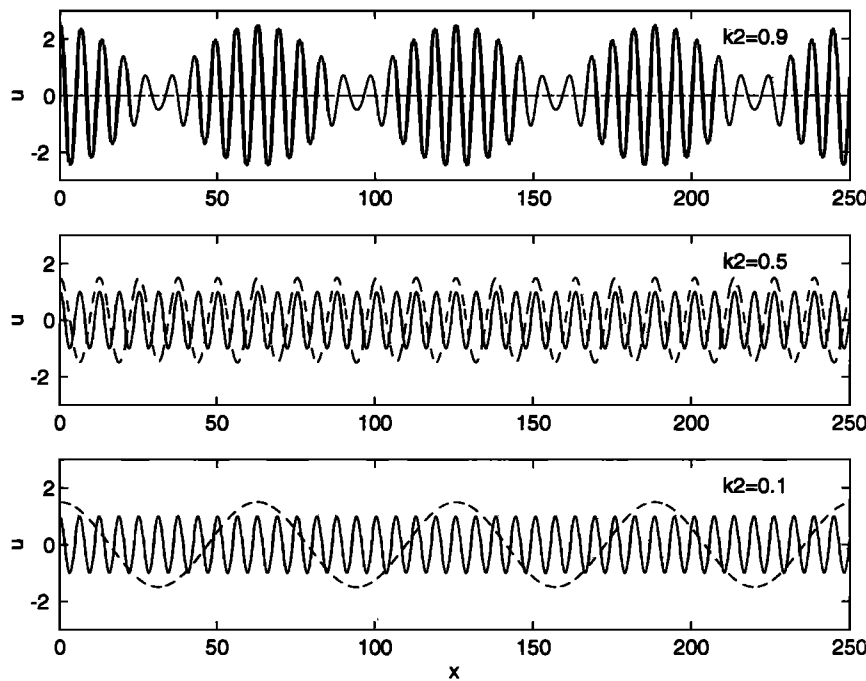
Figure 4. EMD of a superposition of two sinusoidal waves: IMFs decomposed from real signals of Figure 1. The solid lines are the first components of IMFs corresponding to high frequency oscillations. The dashed lines are the second components of IMFs corresponding to low frequency oscillations. In the top panel there is only one IMF since the second IMF vanishes.

slowly variable amplitude. In the later situation the medium is inhomogeneous, and n_r is slowly varying according to (13b).

Since both expressions of the signal may have their own physical origins, the question naturally arises as to which method provides a better spectral decomposition. Can we better identify the actual physics behind the signal by using the EMD method rather than the traditional Fourier analysis? The answer is generally "yes" for nonstationary wave-related data since IMFs derived from the EMD method provide further information on spatial variation in addition to the amplitude and wavenumber for each mode. *Huang et al.* [1997] present many examples extracted from numerical results of nonlinear equation systems and actual data to show the power of the EMD method. In the next section we define a local power spectrum and its marginal distributions which can be applied to analyzing the gravity wave characteristics in the middle atmosphere. The result will help us to understand what mechanism is mainly responsible for the observed universal spectrum of gravity waves in the middle atmosphere.

Our validity condition (10) or (11) provides a precise and quantitative assessment of the separability between the $U_0(\xi)$ spectrum and exp $[i\phi(\xi)]$ spectrum. It also provides a natural link between the numerical derived IMFs and their physical background of dispersive-dissipative wave packets. Furthermore, such a condition is also theoretically crucial for calculating and understanding a well-behaved local wavenumber (or instantaneous frequency). Although the connection between the validity condition of a WKB solution for a wave packet and the separability condition for an analytic signal is natural and inevitable, previous studies in signal processing have apparently missed such a connection. For example, *Boashash* [1992] introduced the notion of monocomponent signals in order to find a well-behaved instantaneous frequency. However, his in-

vertibility condition excludes most of the signals of unmonotonous property which do have a well-defined instantaneous frequency. We have noted that, historically, a WKB solution is mostly used for solving (7) where the independent variable is space, while in signal processing the independent variable is usually time. To conclude this section, we further emphasize here that both expressions of the signal for the case 1 in Figure 1 have their own physical backgrounds. On the basis of the connection between the separation condition of the spectra and the validity condition of the WKB approximation we expect the EMD to provide a natural basis for the analysis of signals which contain dispersive-dissipative wave phenomena.

3. Local Power Spectrum and Its Marginal Distributions

To illustrate how the EMD method may be helpful to understanding the gravity wave characteristics in the middle atmosphere, we need to introduce a distribution function that represents the energy density distribution as a function of space and wavenumber. To show the motivation behind its definition, let us consider an idealized wave packet of velocity perturbation

$$u(z)$$

$$= \begin{cases} \exp{(z/20)} \sin{[200 \exp{(-z/21)}]} & 0 \le z \le 50 \text{ km}; \\ \exp{(2.5)} \sin{[200 \exp{(-z/21)}]} & 50 \le z \le 65 \text{ km}. \end{cases}$$

$$(16)$$

Figure 5 shows the velocity profile $u(z)$, its Hilbert transform $H[u(z)]$, and the wave packet amplitude of the analytic signal $U_0(z)$. Both expression (16) and Figure 5 suggest that the
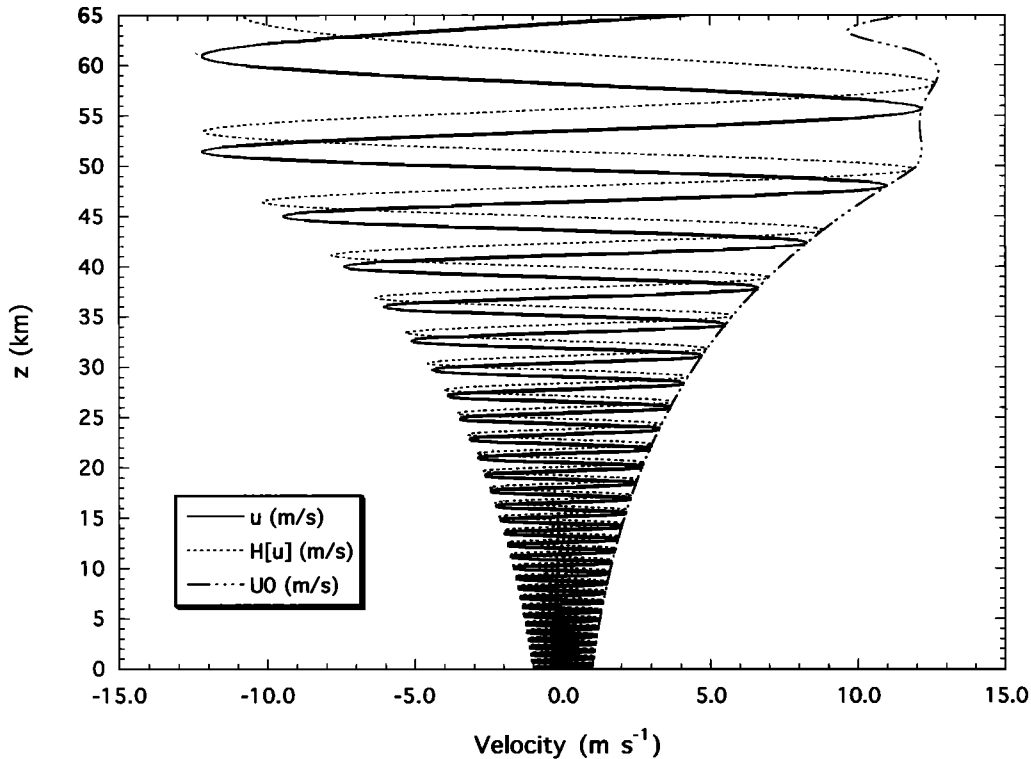
Figure 5. An idealized wave packet of velocity perturbation $u(z)$ (solid line), its Hilbert transform $H[u(z)]$ (dashed line), and the amplitude of the analytic signal $U_0(z)$ (dash-dotted line).

wave packet is an IMF because the validity condition (10) is well satisfied. Figure 6 shows the local vertical wavenumber $m(z)$ and characteristic inverse scale of its amplitude envelope $M(z)$ of the analytic signal based on the definitions (4) and (10), respectively. Two spikes in $m(z)$ and $M(z)$ at 50 km are caused by the discontinuity of du/dz at 50 km. Rapid variations in $M(z)$ close to boundaries are due to the edge effects when performing the Fourier transform to derive $H[u(z)]$ [e.g., *Karl*, 1989]. Furthermore, evaluation of the second derivative in (10) numerically enhances any errors, since it usually involves calculating small differences of large terms. In practice, more realistic criteria of standard deviation and indices of orthogonality [*Huang et al.*, 1997] are used in deriving the IMFs.

By combining Figure 5 and Figure 6 one can establish a one-to-one correspondence at each altitude between the amplitude of the analytic signal $U_0(z)$ (or its square $U_0(z)^2$) and the local wavenumber $m(z)$. The distribution of energy as a function of wavenumber and space, referred to as the Hilbert spectrum, is introduced by *Huang et al.* [1997] to describe the nonlinear and nonstationary effects of various signals. In the present applications of analyzing a gravity wave spectrum a more relevant quantity is the energy spectral density or the power spectrum, $F(m)$, which often shows a near -3 power law at large m. In this section we first introduce a distribution function which we call the local power spectrum. We then suggest that different physical mechanisms for the gravity wave spectrum may lead to different observed structure in the local power spectrum even though the corresponding standard power spectra $F(m)$ are indistinguishable for different processes.

In the work of *Huang et al.* [1997], comparisons are also

made between the EMD method and other time-frequency analysis techniques such as wavelet analysis and the Wigner distribution. Wavelet analysis can be considered as an improved windowed Fourier transform where the scales are adjustable but the basis functions are specified beforehand [e.g., *Daubechies*, 1992; *Kaiser*, 1994]. On the other hand, the Wigner distribution derives internally determined basis functions from the signal itself, but the transform is quadratic rather than linear [*Cohen*, 1995]. The EMD method possesses both merits of linearity and internally determined basis by expressing any signal as a linear superposition of a finite number (J) of analytic signals belonging to their IMFs [*Huang et al.*, 1997]

$$u(z) = \mathrm{Re}\left\{ \sum_{j=1}^{J} U_{0j}(z) \exp\left[i \int^{z} m_j(\tau)\, d\tau \right] \right\}, \qquad (17)$$

where Re { } denotes the real part of the complex signal. Note from (17) that at a given altitude z there exists only a finite numbers of wavenumbers $m_j(z)$. Therefore it is convenient to discretize both space and wavenumber variables according to

$$z_k = z_0 + (k - 1/2)\Delta z \qquad k = 1, 2, \cdots, K. \qquad (18a)$$

$$m_{\ell+1} = m_\ell + \Delta m_\ell \qquad \ell = 1, 2, \cdots, L. \qquad (18b)$$

In the computational algorithm the altitude z will be assigned to z_k if $z_k - \Delta z/2 < z \le z_k + \Delta z/2$. A similar procedure is also applied to discretizing the wavenumber m_j according to the limits in (18b). The local power spectrum at a space-wavenumber point (z_k, m_ℓ) is defined as
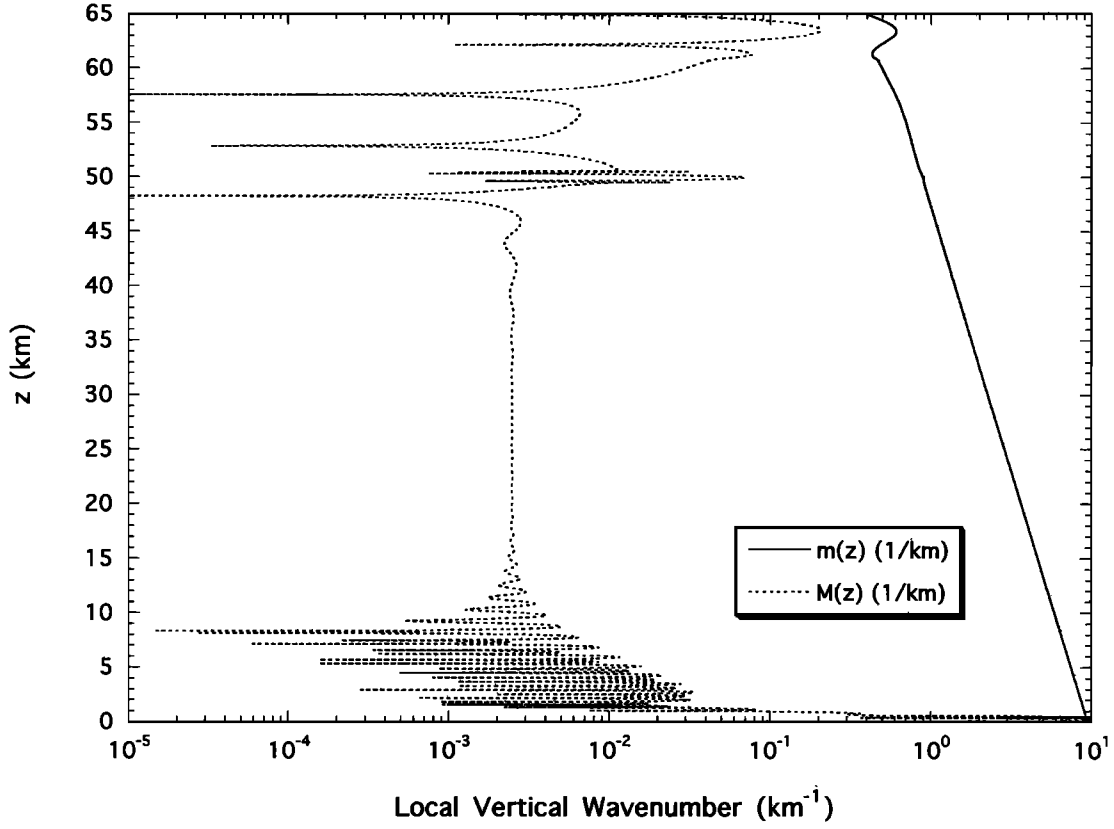
Figure 6. Local vertical wavenumbers $m(z)$ (solid line) and $M(z)$ of the analytic signal in Figure 5 based on the definitions (4) and (10), respectively.

$$P(z_k, m_\ell) = \frac{1}{L} \sum_{j=1}^{J} \frac{[U_{0j}(z_k; m_j(z_k))]^2}{(\Delta m_\ell)} \delta(m_\ell, m_j), \qquad (19)$$

where $\delta(m_\ell, m_j)$ is the Kronecker δ function

$$\delta(m_\ell, m_j) = \begin{cases} 1, & m_\ell = m_j(z_k); \\ 0, & m_\ell \neq m_j(z_k). \end{cases} \qquad (20)$$

In (19) we have written $U_{0j}(z_k)$ as $U_{0j}(z_k; m_j(z_k))$ to indicate that the amplitude is evaluated at $z = z_k$ where the corresponding vertical wavenumber is m_j. Clearly, the local power spectrum $P(z_k, m_\ell)$ is nonnegative and has the conventional units of a spectral density, in this case variance per unit wavenumber. The factor $1/L$ in the definition makes $P(z_k, m_\ell)$ nearly constant for different resolutions of the wavenumber (e.g., $L^* = 2L$ if $\Delta m_\ell^* = \Delta m_\ell/2$). $P(z_k, m_\ell)$ can be considered as a two-dimensional discrete probability density function with the normalization constant

$$N^* = \frac{L}{2K} \sum_{k=1}^{K} \sum_{\ell=1}^{L} P(z_k, m_\ell)\Delta m_\ell. \qquad (21)$$

The two marginal distributions associated with $P(z_k, m_\ell)$ can be defined as

$$F(m_\ell) = \sum_{k=1}^{K} P(z_k, m_\ell) \qquad \ell = 1, 2, \cdots, L; \qquad (22a)$$

$$G(z_k) = \frac{L}{2K} \sum_{\ell=1}^{L} P(z_k, m_\ell)\Delta m_\ell \qquad k = 1, 2, \cdots, K. \qquad (22b)$$

Here the marginal distribution $F(m_\ell)$ is a measure of power spectrum at the wavenumber m_ℓ, while $G(z_k)$ is the variance at the altitude z_k. Under the condition of constant U_{0j} and m_j such as in the last two cases of Figure 1 the normalization constant is the average energy of the real signal $u(z)$; that is,

$$N_u = \frac{1}{K} \sum_{k=1}^{K} u(z_k)^2, \qquad (23)$$

and the marginal distribution $F(m_\ell)$ is the power spectrum of $u(z)$ derived from the Fourier transform. In Plate 1 and Figure 7 we show the local power spectrum $P(z_k, m_\ell)$ and its marginal distribution $F(m_\ell)$, respectively, for the wave packet signal (16) where it has only one IMF ($J = 1$). To demonstrate that the EMD method is superior to the wavelet analysis in this case, we also present in Plate 1 the local power spectrum of wavelet analysis by replacing the amplitude U_0 in (19) with the continuous wavelet transform [Daubechies, 1992]

$$C_0(z_k, m_\ell) = \frac{1}{\sqrt{a}} \int_{-\infty}^{\infty} u(\tau)\psi^*\left(\frac{\tau - z_k}{a}\right) d\tau, \qquad (24)$$

where $a = \pi/m_\ell$ is the scale parameter and the asterisk denotes complex conjugation. The standard Morlet wavelet
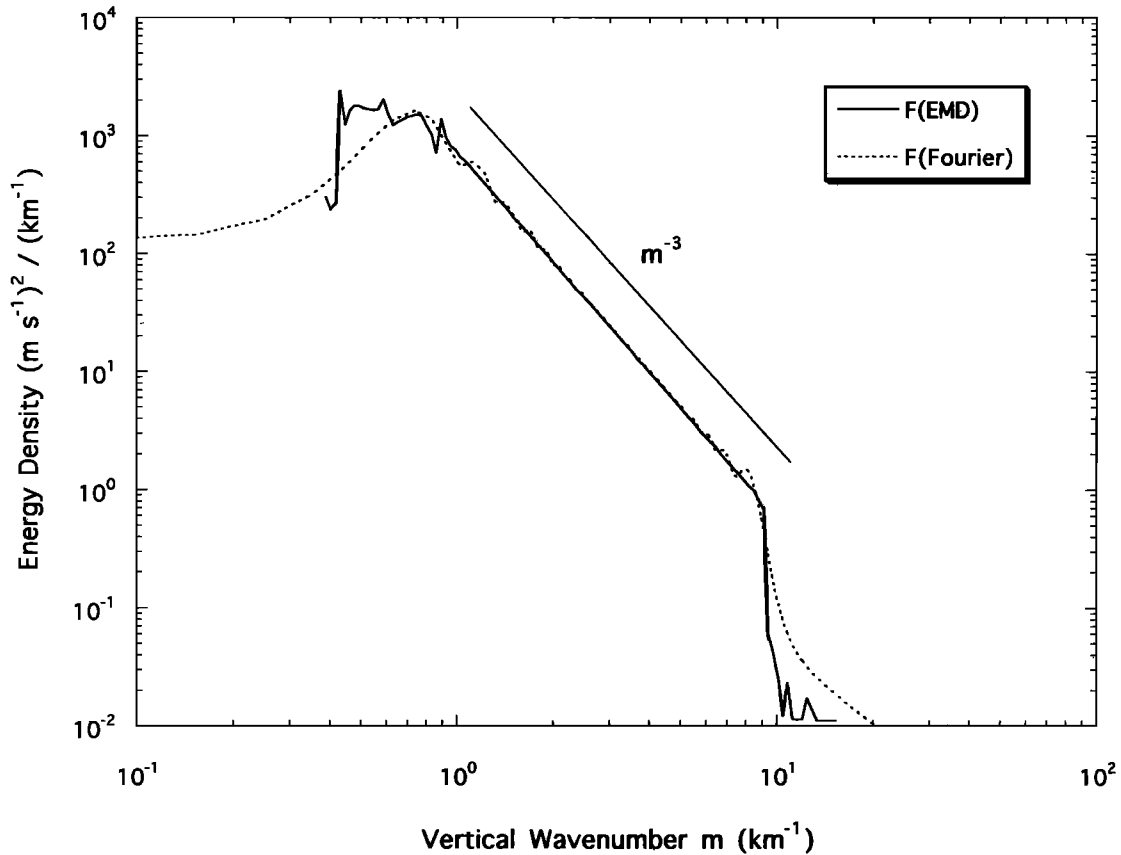
Figure 7. Marginal distribution $F(m_\ell)$ derived from EMD method (solid line) and power spectrum derived from the Fourier transform (dashed line) for the idealized wave packet of Figure 5.

$\psi(\tau) = Ce^{-\tau^2/\alpha^2}(e^{j\pi\tau} - e^{-\pi^2\alpha^2/4})$ with $C = \sqrt{2}/\alpha$ and $\alpha = 4$ has been used in Plate 1. We can see from Plate 1 that although the wavelet analysis provides space-wavenumber information for the signal, the spread of the actual local wavenumber to neighboring heights is unavoidable because $C_0(z_k, m_\ell)$ is a continuous function of space and scale. On the basis of the construction of our idealized waveform (16) we can conclude that such a spread represents an energy leakage in the wavenumber domain due to a less-than-ideal choice for the basis function. Mathematically, this is also due to the admissibility condition of the mother wavelet $\psi(\tau)$ that yields a nonsingular property of $\psi(\tau)$ at $\tau = 0$. More examples of comparison between the EMD method and the wavelet analysis are presented by *Huang et al.* [1997].

From the definition of the local power spectrum we know that each IMF corresponds to one curve in the two-dimensional contour plot $P(z_k, m_\ell)$. As the number J of IMFs increases, one expects a smoother contour plot $P(z_k, m_\ell)$ that may provide a continuous and positive distribution function. However, in real applications, J usually is a small number. For example, to test our sifting program, we applied the EMD method to a data series believed to be most irregular and unpredictable: a 30-year long record of the composite index of The New York Stock Exchange with 7592 trading days. Applying the EMD method to the time series yields only 10 IMFs with timescales ranging from daily variability to an interdecadal oscillation. Therefore, in principle, $P(z_k, m_\ell)$ is discrete in wavenumber (m_ℓ).

It should be noted, however, that a signal or a data series can

be considered as a realization (or a sample) of a physical system. In many applications the actual distribution function $P(z_k, m_\ell)$ of a physical system can be derived by an ensemble average of many independent realizations. Under these circumstances, $P(z_k, m_\ell)$ may show its continuous nature in both space and wavenumber if the actual physical system behaves in such a manner. In the present application to the vertical wavenumber spectrum of gravity waves in the middle atmosphere, $P(z_k, m_\ell)$ is expected (according to some models) to be continuous due to sporadic wave generation, dispersive wave propagation, and nonlinear wave-wave interactions. Other models, however, suggest it may be somewhat more discrete in certain circumstances [e.g., *Alexander*, 1996; *Warner and McIntyre*, 1996].

When there is a frequency or an amplitude modulation in an IMF, the marginal distribution $F_{\text{EMD}}(m)$ and the Fourier spectrum $F_{\text{Fourier}}(m)$ will be different. For example, from (13) we find $F_{\text{EMD}}(m)$ for the IMF in Figure 1 to be

$$F_{\text{EMD}}(\kappa) = \frac{a_2^2 - a_1^2}{\kappa - k_m}, \qquad (25)$$

where the wavenumber κ varies continuously within a wavenumber domain of a finite support $[k_m + k_d(a_2 - a_1), k_m + k_d(a_2 + a_1)]$. Outside such a finite wavenumber support, $F_{\text{EMD}}(m)$ vanishes. On the other hand, the Fourier spectrum $F_{\text{Fourier}}(m)$ of the same signal consists of two spectral lines located at $\kappa = k_1$ and $\kappa = k_2$, respectively. As we have already discussed in the previous section, either form of $F_{\text{EMD}}(\kappa)$ or $F_{\text{Fourier}}(m)$ may correctly correspond its own

physical process. One usually cannot identify the actual physical process based on differences between $F_{EMD}(m)$ and $F_{Fourier}(m)$ alone. This example also shows the importance of choosing different spectral analysis tools in analyzing the data. The Fourier spectrum resolves two harmonics since it assumes that the series is a superposition of infinite constant amplitude harmonics. Thus the only way for it to represent a slowly varying amplitude is to split it up into two harmonics which beat when retransformed. The EMD method avoids this and gives a direct picture of amplitude modulation of the wave packet. However, conversely, the EMD method cannot resolve two closely spaced harmonics due to the acceptable separability criterion (10) or (11). In the real applications, such as in the present situation, when a data series is associated with physical processes which can be approximated by the wave equation (7), the EMD method is expected to yield a better decomposition.

For a real signal with multi-IMFs and a finite length its $F_{EMD}(m)$ will still be a continuous function of a finite wavenumber support because the local wavenumbers are ·continuous functions of space. On the other hand, the Fourier spectrum of a finite length signal $F_{Fourier}(m)$ will be unlimited in wavenumber space. The cutoff wavenumbers are determined mainly by how the continuous signal is sampled [e.g., Karl, 1989; Harris, 1978]. It is a notoriously difficult problem to find a positive space-wavenumber (or time-frequency) distribution that satisfies the specified marginal distributions [Cohen, 1995]. Because our marginal distributions (22) are defined by the nonnegative local power spectrum, the required condition of a two-dimensional probability density is satisfied automatically. Although our marginal distributions, such as $F_{EMD}(m)$, are different from the marginal distributions specified in the usual time-frequency analysis [Cohen, 1995], such as $F_{Fourier}(m)$, the marginal distributions are physically meaningful as we discussed in the last section. Therefore the local power spectrum $P(z_k, m_\ell)$ is clearly an appropriate distribution function.

It is also noted that the Fourier spectrum $F_{Fourier}(m)$ derived in turbulence studies also represents an ensemble average of many independent realizations. However, for homogeneous turbulence where the flows are considered to be stationary in time the ergodic theorem ensures that the ensemble average is the same as the average over a long data series [e.g., Panchev, 1971; Frisch, 1995]. Examining Figure 5 clearly shows that the wave packet is not a stationary signal. Therefore additional cautions should be exercised to interpret $F_{Fourier}(m)$ when it is derived from only a few data series.

4. Gravity Wave Characteristics in the Middle Atmosphere

On returning to Figure 7 we are now in a position to demonstrate some of the usefulness of the EMD method and the local spectrum $P(z_k, m_\ell)$ in the analysis of gravity-wave data in the middle atmosphere. We have already discussed the differences between $F_{EMD}(m)$ and $F_{Fourier}(m)$ in terms of their physical interpretations. The most significant difference is that they use a different set of basis functions to decompose the data, as shown in Figure 7. However, within the major part of their common wavenumber domain, $F_{EMD}(m)$ is very close to $F_{Fourier}(m)$ since both functions represent the wave energy per wavenumber. In the present example of the idealized wave packet shown in Figure 5, both $F_{EMD}(m)$ and $F_{Fourier}(m)$ exhibit a -3 slope in their Log (F)-log (m) plots. This is consistent with the vertical wavenumber spectra derived from

many observations [e.g., VanZandt, 1982; Tsuda et al., 1989; Wu and Widdel, 1989, 1992; Senft and Gardner, 1991]. Although the -3 slope of $F_{EMD}(m)$ and $F_{Fourier}(m)$ in the present example can be considered as coincidental, the idealized wave packet shown in Figure 5 resembles observations in several respects. First, observations also show that the amplitude of internal gravity waves increases exponentially with altitude [e.g., Hirota and Niki, 1985] but that wave amplitudes tend to be constant with height in the mesosphere [see, e.g., Tsuda et al., 1994, Figure 7]. The first observation is consistent with the notion that the density effect of the background atmosphere amplifies the upward propagating gravity waves [Hines, 1960], whereas the second observation is consistent with the perceived "saturation" of wave amplitude at mesosphere heights. Second, changes of refraction index associated with background wind shear and varying static stability also alters the vertical wavenumber [e.g., Bleistein, 1984; Bretherton, 1966; Zhu, 1987; Marks and Eckermann, 1995].

The near -3 slope of the vertical wavenumber spectrum for the gravity waves in the middle atmosphere was first noted by VanZandt [1982]. He suggested that such a universal spectrum in the atmosphere might be similar to the universal spectrum introduced by Garrett and Munk [1972, 1975] to describe oceanic internal waves. Since then, many different theories have been proposed to explain the apparent universal -3 power law for the vertical wavenumber spectrum [e.g., Dewan and Good, 1986; Smith et al., 1987; Weinstock, 1990; Hines, 1991; Gardner, 1994; Zhu, 1994]. We can divide different mechanisms into two arbitrary categories: linear versus nonlinear. A linear mechanism usually suggests that there is a characteristic (or dominant) wave component with the amplitude growing with altitude due to the density effect. However, the characteristic wave component grows at a rate smaller than the inverse of the air density due to the existence of damping mechanisms such as wave breaking and radiative damping. An ensemble average of all characteristic wave components forms a near -3 power spectrum. The amplitude of a characteristic wave is also strongly controlled by the different generation mechanisms [e.g., Lindzen, 1984; Zhu and Holton, 1987]. In nonlinear mechanisms all wave components interact in a way that in some models cascades the larger-scale waves to smaller scales [e.g., Dewan, 1994].

Even though both marginal distributions of linear and nonlinear mechanisms may yield the same form of power law $F_{EMD}(m) \sim m^{-p}$ with $p \sim 3$, its local power spectra $P(z_k, m_\ell)$ will exhibit different structures in terms of their spatial and wavenumber distributions. In the case that a single wave component dominates the whole spectrum one expects $P(z_k, m_\ell)$ to be sharply peaked along one line as in Plate 1. Furthermore, the strengths and mechanisms that excite gravity waves at different locations and altitudes differ significantly. As a consequence, at a given altitude z_k, $P(z_k, m_\ell)$ may not have an m^{-p} power spectrum as a function of m_ℓ. On the other hand, when the nonlinear cascade process becomes dominant, one may expect a universal m^{-p} power spectrum in m_ℓ that is independent of location and altitude.

To test which mechanism is closer to the observations, we present in Plate 2a the local power spectra $P(z_k, m_\ell)$ calculated from 38 horizontal wind profiles (u, v) obtained during the Dynamics Adapted Network for the Atmosphere (DYANA) campaign, carried out in January through March 1990 in the northern hemisphere [Offermann, 1994]. All 38 profiles were derived by tracking passive falling spheres released from rock-
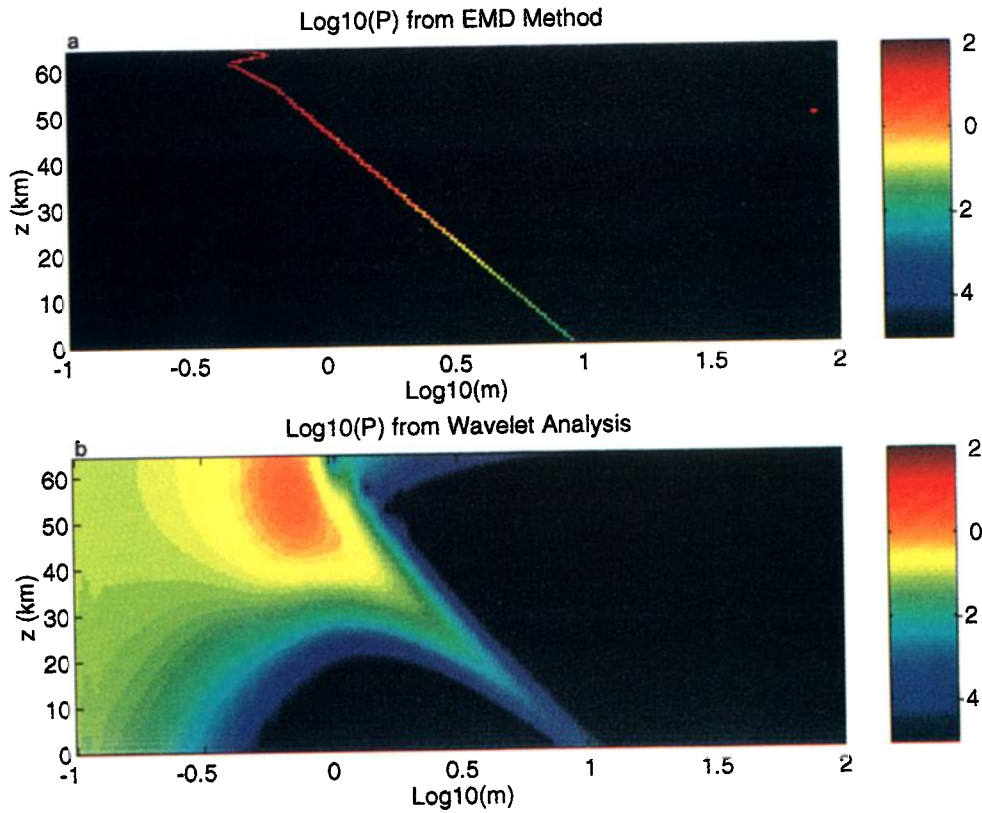
Plate 1. Logarithm of local power spectrum, $\text{Log}_{10} [P(z_k, m_\ell)]$, of the idealized wave packet of Figure 5: (top) $P(z_k, m_\ell)$ is calculated by (19) from the EMD method; (bottom) $P(z_k, m_\ell)$ is calculated by (19) from the wavelet analysis with U_0 in (19) replaced with C_0 in (24). The color scheme is made to "saturated" below the value of -5 to accentuate significant wave energy in the neighborhood of the local wavenumber.
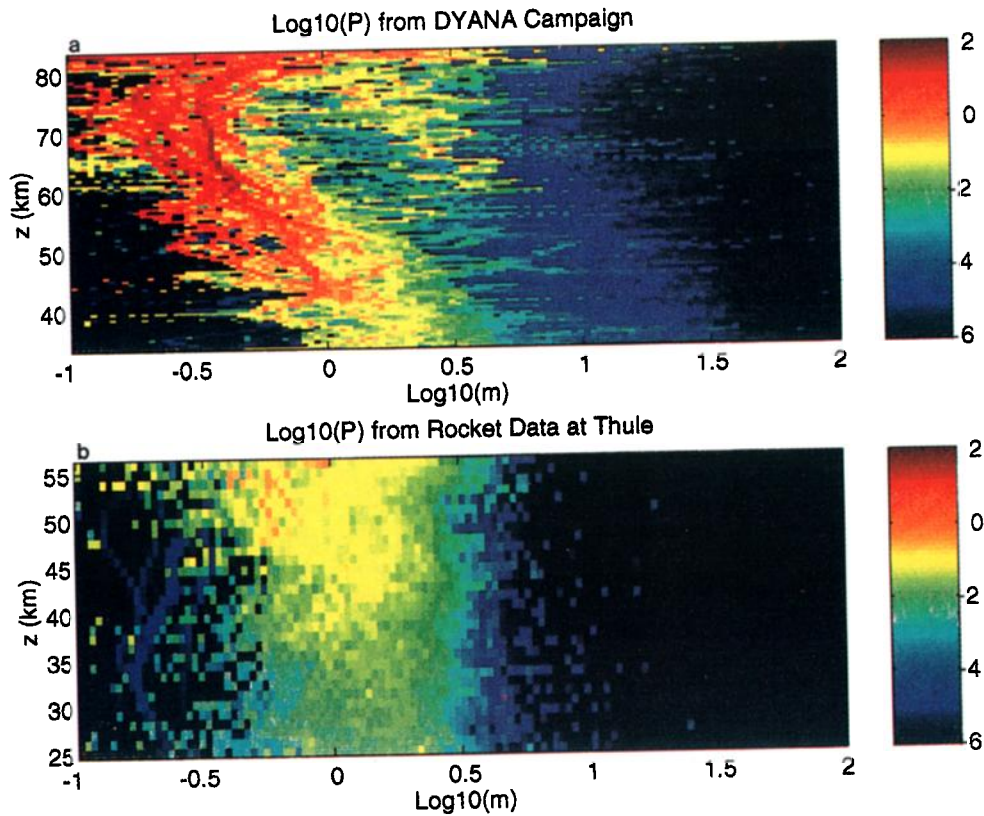

Plate 2. Logarithm of local power spectrum, $\text{Log}_{10} [P(z_k, m_\ell)]$, of the observed horizontal wind fields: (top) from DYANA campaign (69°N, 16°E and 44°N, 1°W) and (bottom) from long-term rocket soundings at Thule (77°N, 69°W).

ets at an apogee ~95 km, with data available in an altitude region between 33 and 91 km. Fifteen rockets were launched at Biscarosse (France; 44°N, 1°W), and 23 rockets were launched at Andøya (Norway; 69°N, 16°E). It is found from Plate 2a that the local power spectra $P(z_k, m_\ell)$ is peaked at a wavenumber m^* which varies with altitude

$$m^*(z) = \begin{cases} 2.0 \exp\left[-(z - 40)/19.5\right] & z \le 78 \text{ km}; \\ 0.28, & z > 78 \text{ km}. \end{cases} \quad (26)$$

Here we define m^* as the characteristic vertical wavenumber at which the local power spectra reach their maxima. Such a definition is also consistent with the m^* defined by Smith et al. [1987] where m^* is also the lower cutoff wavenumber for a m^{-3} region in the power spectrum of gravity-wave-induced horizontal velocity perturbations.

A striking feature shown in Plate 2a is a disjointed secondary maximum in $P(z_k, m_\ell)$ above 60 km with its peak vertical wavenumber $m^\dagger$ 1 order of magnitude greater than the primary m^* defined by (26). The clear separation between m^* and $m^\dagger$ shown in $P(z_k, m_\ell)$ suggests that there exists two different physical processes above 60 km. Because of the atmospheric density effect, the response function of a falling sphere to high wavenumber wind fluctuations decreases rapidly with the altitude [Hass and Meyer, 1987]. Therefore the secondary maximum in $P(z_k, m_\ell)$ above 60 km will correspond to very strong gravity wave activities if it were due to wind fluctuations. We believe that this secondary maximum in $P(z_k, m_\ell)$ is due to sphere vibrations caused by shock waves emitted from the falling spheres [e.g., Lighthill, 1978; Landau and Lifshitz, 1987].

It can be easily shown that a free-falling sphere reaches the speed of Mach 1 (speed of sound $\approx 300 \text{ ms}^{-1}$ around the winter mesopause) at a traveling distance of $\gamma H/2$ when initially released at rest, where $\gamma = c_p/c_v = 1.4$ is the ratio of the specific heats and H is the scale height. At a certain stage the falling sphere will reach a terminal velocity that decreases with the decreasing altitude because the air drag increases [Miller, 1969]. Eckermann and Vincent [1989] estimated that the terminal velocity at 60 km is about Mach 0.5 (150 ms^{-1}). Therefore we expect spheres to fall supersonically above ~65 km. For a sphere falling at a speed greater than Mach 1 the shock waves are emitted downward within a cone with an acute angle of $\cos^{-1}(1/M)$, where M is the Mach number. The emission of shock waves may cause the sphere to experience a jolt at high frequency which results in a high wavenumber oscillation in the retrieved vertical profile at that altitude. Between 60 and 65 km the sphere could still suffer a forced oscillation due to the catch-up of the shock waves previously emitted above 65 km. It should be noted that because of the atmospheric density effect, the secondary peak wavenumber $m^\dagger$ tilts with height in a form similar to m^*. Such an unrealistic feature about the wind profiles will be difficult to identify by conventional Fourier analysis.

To quantitatively examine which mechanism is more responsible for a possibly observed near -3 slope in the Fourier analysis [e.g., Zhu, 1994], we show in Figure 8 the marginal distributions at different altitude ranges. We see from the figure that the marginal distribution for the entire region from 35 to 85 km, $F_{\text{All}}(m)$, shows an overall near -3 slope except around 4 km^{-1} where the localized energy density bump due to the shock waves produces to a -2 slope. Again, without the knowledge of the local power spectrum it will be difficult to

realize two distinct processes that are responsible for the apparently smooth -2 slope in the marginal distribution or the power spectrum from Fourier analysis. By looking into individual contributions from the local power spectra to the marginal distribution we can identify some individual physical processes that are responsible for the form of the marginal distribution, $F_{\text{All}}(m)$.

Next, we calculate the marginal distribution for the entire region but contributed spectrally only from the following wavenumber band, $F_{m^*}(m)$,

$$\text{Log}_{10}(m^*(z)) - 0.25 \le \text{Log}_{10}(m) \le \text{Log}_{10}(m^*(z)) + 0.25, \quad (27)$$

where $m^*(z)$ is defined by (26). The result is also plotted in Figure 8. We see that when the vertical wavenumber $m < 0.1$ km^{-1} (or vertical wavelength $L_z > 63$ km), the two marginal distributions are almost identical indicating that characteristic gravity waves parameterized by a single wavenumber contain most of the energy. Such a picture is consistent with the "quasi-monochromatic" parameterization of gravity wave processes advocated by Yamanaka and Fukao [1994] where the dominant vertical wavenumbers have form similar to (26). Furthermore, the marginal distribution $F_{m^*}(m)$ is much closer to an m^{-3} power law than $F_{\text{All}}(m)$. Returning to Plate 2a, we now can clearly identify that the small bump of a local m^{-2} power law in $F_{\text{all}}(m)$ is caused by a secondary maximum in $P(z_k, m_\ell)$ above 60 km that has a vertical wavenumber $m^\dagger \sim 2$ km^{-1} ($L_z \sim 3$ km). To exclude the nonstationary effects of the atmospheric density and stratification, we calculate and plot in Figure 8 the marginal distributions of 3 km slabs centered at different altitudes $F_{\text{slab}}(m)$. After excluding the unphysical bumps above 60 km, we see that when $m > 3$ km^{-1} ($L_z < 2$ km), the marginal distributions for the slabs generally exhibit a power law distribution m^{-p} with $p = 2 \sim 4$. This result is also consistent with the wavelet spectrum analysis of the lower stratospheric temperature and wind observations [Sato and Yamada, 1994]. When $m < 3$ km^{-1} ($L_z > 2$ km), the slab marginal distributions show a distinct feature of systematic shifting of the peak $F_{\text{slab}}(m)$ toward smaller vertical wavenumber as the altitude increases. The shifting is consistent with variation of the characteristic vertical wavenumber along the altitude, as indicated in Figure 8. However, there appears no universal power law that can fit $F_{\text{slab}}(m)$ for $m^* < m < 3$ km^{-1} even though a -3 power law exists in $F_{\text{all}}(m)$ in this wavenumber range.

In Plate 2a we also show the local power spectra $P(z_k, m_\ell)$ calculated from 175 horizontal wind profiles (u, v) from meteorological rocket soundings at Thule (77°N, 69°W). The data cover the altitude range from 20 to 60 km with 1 km vertical resolution [Eckermann et al., 1994]. Here, we see again a relatively concentrated $P(z_k, m_\ell)$ around $m = 1$ km^{-1} ($L_z = 6.3$ km). Furthermore, since more wind profiles have been used, $P(z_k, m_\ell)$ is smoother than in Plate 2a. However, because of the lower resolution of the data, many features of $P(z_k, m_\ell)$ at higher vertical wavenumbers may have been lost.

5. Hodographic Analysis of Characteristic Gravity Waves

We have established in section 2 a close connection between the WKB wave packet solutions of a dispersive-dissipative physical system and IMFs derived from the EMD method. In
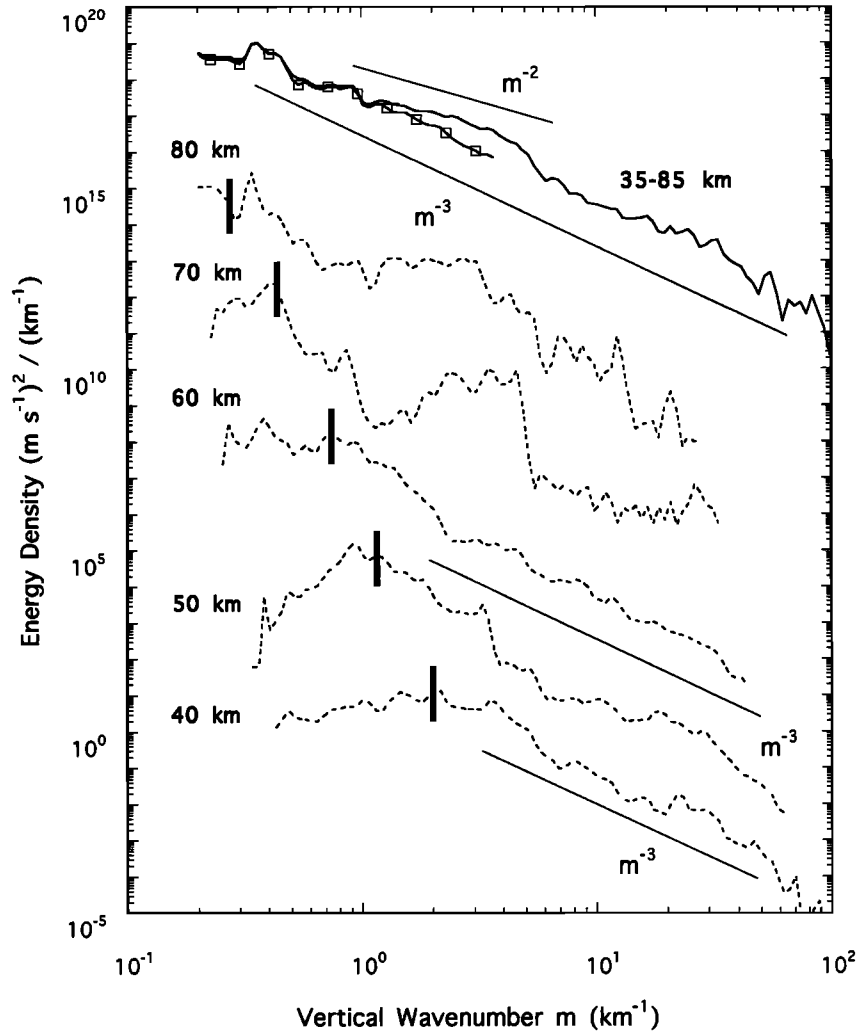
Figure 8. Marginal distributions at different altitudes calculated from Plate 2a. Two solid lines are the marginal distributions in the entire region ranging from 35 to 85 km. The one with the open squares is calculated by setting $P(z_k, m_\ell) = 0$ outside the spectral band of characteristic vertical wavenumber as defined by (27). The dashed lines are the marginal distributions within a 3 km slab centered at the altitude as indicated. The thin solid straight lines represent either m^{-3} or m^{-2} power law. Five vertical parallel bars mark the characteristic vertical wavenumbers m^* at different altitudes. All the curves except the one at 40 km have been consecutively moved up by 3 orders of magnitude to avoid clustering.

the work of *Huang et al.* [1997], several examples are presented to show that many derived IMFs have their own physical interpretations. Here we show for the DYANA campaign data that one IMF can be identified as a major component of upward propagating inertia gravity waves in the middle atmosphere.

In falling sphere experiments the wind and temperature profiles are extracted from the retrieved atmospheric density profiles. To exclude background mean and planetary wave scale perturbations and to account for the strong nonstationarity of the instrument response function [*Hass and Meyer*, 1987], we first employ a band-pass filter to decompose a wind profile, u or v, into background and perturbation components

$$u(z) = U(z) + u'(z). \tag{28}$$

We use a 101 points Savitzky-Golay filter corresponding to a 2 km window width [*Press et al.*, 1992, p. 644]. The EMD method is applied to the perturbation $u'(z)$ to derive all of its IMFs

$$u'(z) = \sum_{j=1}^{J} u_j(z)$$

$$= \mathrm{Re}\left\{ \sum_{j=1}^{J} U_{0j}(z) \exp\left[i \int^{z} m_j(\tau)\, d\tau \right] \right\}, \tag{29}$$

whereas for the background component $U(z)$, EMD method is used to derive one IMF denoted as u_g

$$U(z) = u_b(z) + u_g(z) = u_b(z)$$

$$+ \mathrm{Re}\left\{ U_{0g}(z) \exp\left[i \int^{z} m_g(\tau)\, d\tau \right] \right\}. \tag{30}$$

Here the residual in the low wavenumber component $u_b(z)$ is considered as the background mean and planetary wave scale perturbations. We apply the same procedure to the meridional
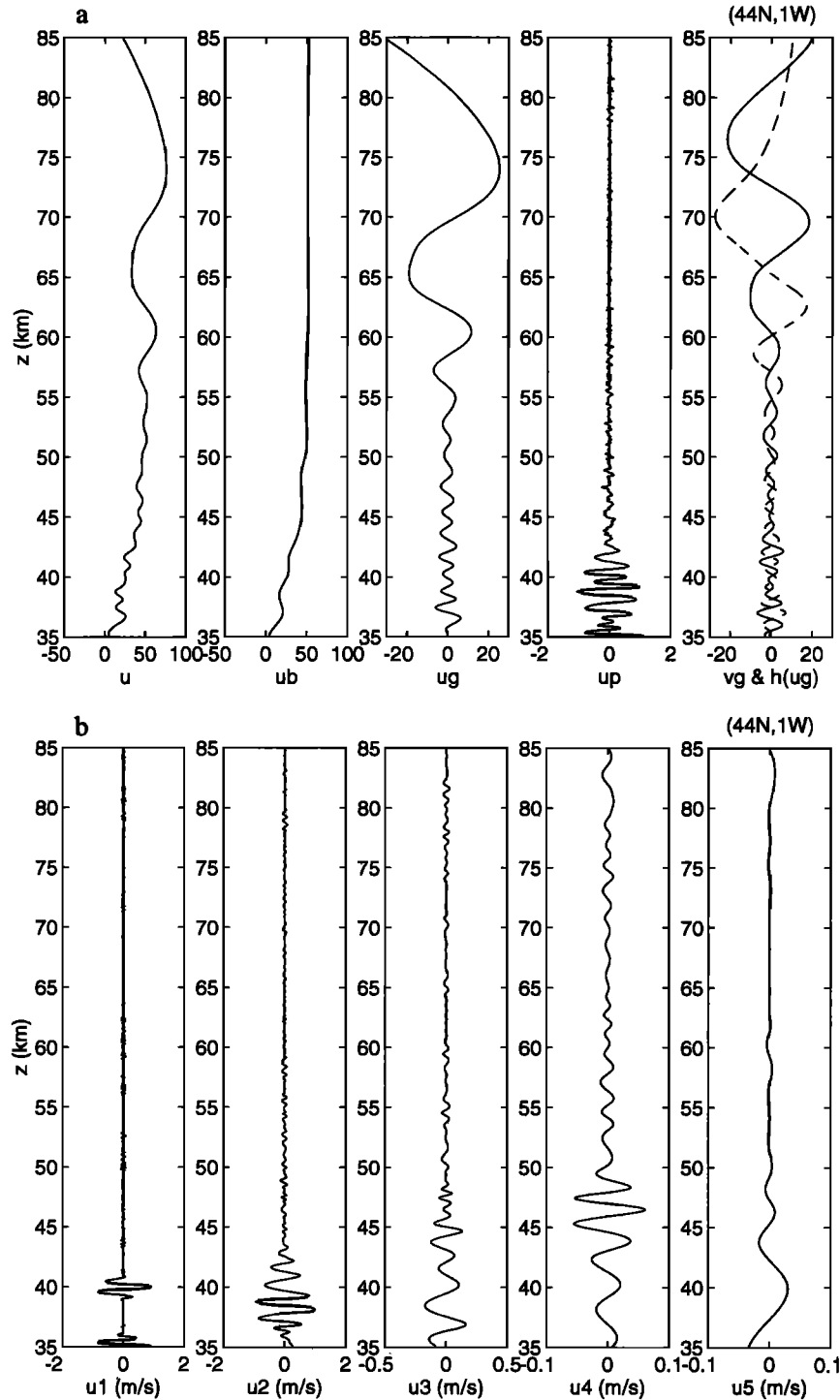
Figure 9. (a) Zonal wind u observed at Biscarosse (France; 44°N, 1°W) and its decomposition by (28) and (29): u_b, u_g, and u'. In the last strip, solid line and dashed line denote v_g and $H(u_g)$, respectively. (b) Five IMFs for the high-pass zonal wind u' shown in Figure 9a.

components $v(z)$. Our local power spectra presented in Plate 2 are calculated based on all the IMFs $u_g(z)$ and $\Sigma\ u_j(z)$.

In Figures 9 and 10 we present two examples of decomposing the original wind profiles into various components u_b, u_g, u', and u_j. We can see from figures that u_g contains most of the wave energy for the disturbances of scales less than those of u_b. The structures of u_g in these two examples resemble upward propagating gravity waves with certain wavenumber

and amplitude modulations. It is well known that at the mid and high latitudes, horizontal wind perturbations of a pure gravity wave component show elliptical rotation with height [e.g., *Hirota and Niki*, 1985]. This is because the polarization relation of inertia gravity waves renders a constant phase shift between u_g and v_g components [e.g., *Gossard and Hooke*, 1975]. Furthermore, the Hilbert transform of a signal also produces a 90° phase shift from the original data [e.g.,
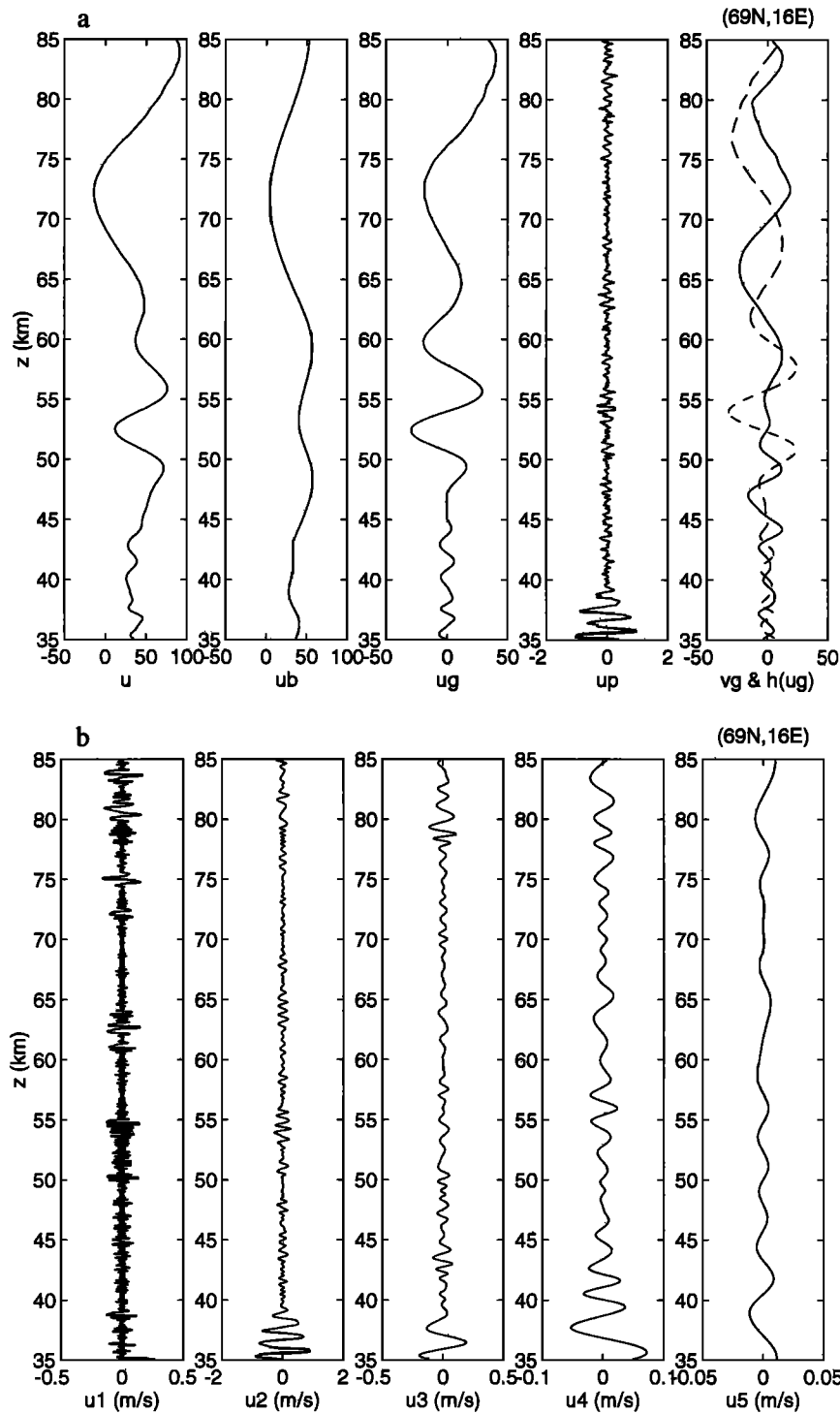
Figure 10. Same as Figure 9, except for a wind profile at Andøya (Norway; 69°N, 16°E).

Bracewell, 1986; *Karl*, 1989]. In the last strips of Figures 9a and 10a we also show v_g and $H(u_g)$ profiles. Clearly, v_g and $H(u_g)$ exhibit a near-constant phase difference in the majority of the region, strongly suggesting that (u_g, v_g) are representing a near monochromatic inertia gravity wave.

A convenient and quantitative way to describe the wave propagation characteristics is to use four Stokes parameters (I, D, P, Q). The Stokes parameters were first introduced for studying the gravity waves by *Vincent and Fritts* [1987]. *Ecker-*

mann and Vincent [1989] suggested that the Stokes parameters could be calculated spectrally. Recently, *Eckermann* [1996] investigated the relationships among the Stokes parameters, rotary spectra, and cross-spectral methods. Given the Stokes parameters, some gravity wave characteristics such as the phase difference δ_g and the major axis orientation τ_g can be derived [*Eckermann and Vincent*, 1989]
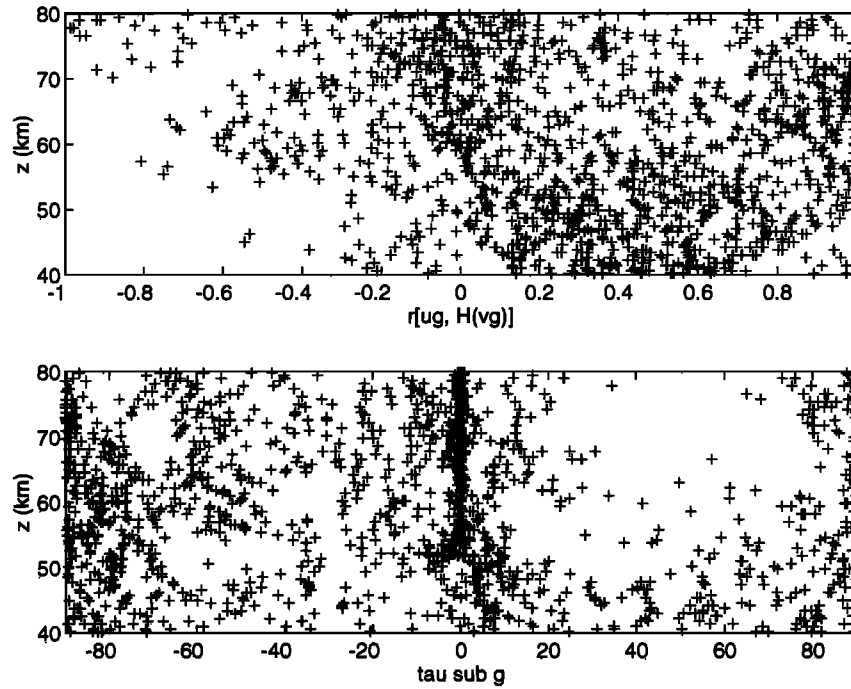
$$\delta_g = \tan^{-1}(Q/P), \tag{31}$$

Figure 11. Correlation coefficient Corr $[u_g, H(v_g)]$ and the major axis orientation τ_g derived for all 38 wind profiles.

$$\tau_g = 1/2\ \tan^{-1}(P/D). \tag{32}$$

In the above the axial anisotropy D and the linear polarization P can be straightforwardly calculated from velocity profiles [*Eckermann*, 1996]

$$D = \overline{u_g^2} - \overline{v_g^2}, \tag{33}$$

$$P = 2\overline{u_g v_g}, \tag{34}$$

where overbars denote height averaging of the velocity profiles over an altitude range longer than local vertical wavelengths. With the help of the Hilbert transforms of u_g or v_g the phase difference δ_g can be calculated by

$$\sin \delta_g = \text{Corr}\ [u_g, H(v_g)] = -\text{Corr}\ [v_g, H(u_g)], \tag{35}$$

where the correlation function is defined as

$$\text{Corr}\ [u_g, H(v_g)] = \frac{\overline{u_g H(v_g)}}{(\overline{u_g^2}\ \overline{H^2(v_g)})^{1/2}}. \tag{36}$$

Combining (31) and (35) gives the circular polarization parameter Q. This technique of using the covariance of u' and $H(v')$ for calculating Q was also indicated by *Eckermann et al.* [1994] for the total perturbation velocities (u', v'). Such an approach leads to a physically meaningful Q only when there exists a dominant wave component, as indicated by *Vincent and Fritts* [1987] by a condition of sufficiently narrow bands. Here our (u_g, v_g) profiles are derived from the EMD method that guarantees narrow bands. Therefore present $\sin \delta_g$ or Q derived from (35) is accurate. The phase difference δ_g is related to the gravity wave parameters through [*Zhu*, 1987]

$$\sin \delta_g = \frac{f\omega K^2}{\sqrt{[(k\omega)^2 + (\ell f)^2][(\ell\omega)^2 + (kf)^2]}}, \tag{37}$$

where f is the Coriolis parameter, ω is the Doppler-shifted frequency, (k, ℓ) is the horizontal wavenumber vector, and $K^2 = k^2 + \ell^2$. A positive correlation between u_g and $H(v_g)$ corresponds to upward propagating gravity waves in the northern hemisphere. Furthermore, (37) indicates that $|\sin \delta_g| \to 1$ under either one of the following three conditions: $k \to 0$, $\ell \to 0$, or $\omega \to f$. For a fast traveling gravity wave with $\omega \to N \gg f$, then $|\sin \delta_g| \ll 1$ which corresponds to a linear polarized wave motion due to the weak inertial effect.

Figure 11 shows the scattered plots of Corr $[u_g, H(v_g)]$ and the major axis orientation τ_g, and we see that the upward propagating gravity waves are dominant in the middle atmosphere which is consistent with many previous studies [e.g., *Vincent*, 1984; *Hirota and Niki*, 1985]. Furthermore, Figure 11b indicate that above ~50 km there is an anisotropy in the horizontal directions of wave propagation with an NW/SE bias. Such an NW/SE bias in the northern hemisphere winter was also detected previously by *Hamilton* [1991].

6. Conclusions

We have explored the recently developed Empirical Mode Decomposition (EMD) method and applied it to analyzing gravity wave characteristics in the middle atmosphere. An important connection is established in this paper between the fundamental Intrinsic Mode Functions (IMFs) derived from the EMD method and WKB solutions of a dispersive-dissipative wave equation. Since the WKB solution corresponds to a wave packet whose structure and wavenumber are internally determined from the data, the IMF representations of wind profiles provide useful insights into physical processes in the middle atmosphere where the dispersive-dissipative wave phenomena are dominant. The positive distribution function $P(z_k, m_\ell)$ introduced in section 3 provides a quantitative

description of space-wavenumber localization of a data series. Application to the observed wind profiles derived from the DYANA campaign leads to an identification of what appear to be unphysical small scale oscillations by falling spheres embedded in the wind profiles above 60 km. It is found that for the vertical wavenumber $m \leq 3 \text{ km}^{-1}$ ($L_z \geq 2$ km) the previously observed m^{-3} Fourier spectra could be a manifestation of a linear wave packet whose characteristic vertical wavenumber decreases with altitude. For small vertical scale disturbances with $m > 3 \text{ km}^{-1}$ ($L_z < 2$ km) a near -3 slope in the marginal distribution exists locally in the middle atmosphere with a great degree of universality, suggesting that nonlinear energy cascade processes might dominate the spectral formation. It is also shown that the hodographic analysis by the Stokes parameters advocated by *Vincent and Fritts* [1987] and *Eckermann and Vincent* [1989] can also be applied to the IMFs derived from the EMD method.

References

Abramowitz, M. J., and I. A. Stegun, *Handbook of Mathematical Functions*, Dover, Mineola, N. Y., 1965.

Alexander, M. J., A simulated spectrum of convectively generated gravity waves: Propagation from the tropopause to the mesopause and effects on the middle atmosphere, *J. Geophys. Res.*, *101*, 1571–1588, 1996.

Bacmeister, J. T., S. D. Eckermann, P. A. Newman, L. Lait, K. R. Chan, M. Loewenstein, M. H. Proffitt, and B. L. Gary, Stratospheric horizontal wavenumber spectra of winds, potential temperature, and atmospheric tracers observed by high-altitude aircraft, *J. Geophys. Res.*, *101*, 9441–9770, 1996.

Bacmeister, J. T., S. D. Eckermann, L. Sparling, K. R. Chan, M. Loewenstein, and M. H. Proffitt, Analysis of intermittency in aircraft measurements of velocity, temperature and atmospheric tracers using wavelet transforms, in *Gravity Wave Processes and Their Parameterization in Global Climate Models*, *NATO ASI Ser.*, vol. 1, edited by K. Hamilton, pp. 85–102, Springer-Verlag, New York, 1997.

Bender, C. M., and S. T. Orszag, *Advanced Mathematical Methods for Scientists and Engineers*, 593 pp., McGraw-Hill, New York, 1978.

Bleistein, N., *Mathematical Methods for Wave Phenomena*, 341 pp., Academic, San Diego, Calif., 1984.

Boashash, B., Estimating and interpreting the instantaneous frequency of a signal, 1, Fundamentals, *Proc. IEEE*, *80*, 520–538, 1992.

Bracewell, R. N., *The Fourier Transform and Its Applications*, 2nd ed., 474 pp., McGraw-Hill, New York, 1986.

Bretherton, F. P., The propagation of groups of internal gravity waves in a shear flow, *Q. J. R. Meteorol. Soc.*, *92*, 466–480, 1966.

Broutman, D., The focusing of short internal waves by an inertial wave, *Geophys. Astrophys. Fluid Dyn.*, *30*, 199–225, 1984.

Cohen, L., *Time-Frequency Analysis*, 299 pp., Prentice-Hall, Englewood Cliffs, N. J., 1995.

Daubechies, I., *Ten Lectures on Wavelets*, 357 pp., SIAM, Philadelphia, Pa., 1992.

Davis, A., A. Marshak, W. Wiscombe, and R. Cahalan, Scale invariance of liquid water distributions in marine stratocumulus, I, Spectral properties and stationarity issues, *J. Atmos. Sci.*, *53*, 1538–1558, 1996.

Dewan, E. M., The saturated-cascade model for atmospheric gravity

wave spectra and the wavelength-period (W-P) relations, *Geophys. Res. Lett.*, *21*, 817–820, 1994.

Dewan, E. M., and R. E. Good, Saturation and the "universal" spectrum for vertical profiles of horizontal scalar winds in the atmosphere, *J. Geophys. Res.*, *91*, 2742–2748, 1986.

Eckermann, S. D., Effects of nonstationarity on spectral analysis of mesoscale motions in the atmosphere, *J. Geophys. Res.*, *95*, 16,685–16,703, 1990.

Eckermann, S. D., Ray-tracing simulation of the global propagation of inertia gravity waves through the zonally averaged middle atmosphere, *J. Geophys. Res.*, *97*, 15,849–15,866, 1992.

Eckermann, S. D., On the observed morphology of gravity-wave and equatorial-wave variance in the stratosphere, *J. Atmos. Terr. Phys.*, *57*, 105–134, 1995a.

Eckermann, S. D., Effect of background winds on vertical wavenumber spectra of atmospheric gravity waves, *J. Geophys. Res.*, *100*, 14,097–14,112, 1995b.

Eckermann, S. D., Hodographic analysis of gravity wave: Relationships among Stokes parameters, rotary spectra, and cross-spectral methods, *J. Geophys. Res.*, *101*, 19,169–19,174, 1996.

Eckermann, S. D., and W. K. Hocking, The effect of superposition on measurements of atmospheric gravity waves: A cautionary note and some reinterpretations, *J. Geophys. Res.*, *94*, 6333–6339, 1989.

Eckermann, S. D., and C. J. Marks, An idealized ray model of gravity wave-tidal interactions, *J. Geophys. Res.*, *101*, 21,195–21,212, 1996.

Eckermann, S. D., and R. A. Vincent, Falling sphere observations of anisotropic gravity wave motions in the upper stratosphere over Australia, *Pure Appl. Geophys.*, *130*, 509–532, 1989.

Eckermann, S. D., I. Hirota, and W. K. Hocking, Gravity wave and equatorial wave morphology of the stratosphere derived from long-term rocket soundings, *Q. J. R. Meteorol. Soc.*, *121*, 149–186, 1994.

Einaudi, F., and C. O. Hines, WKB approximation in application to acoustic-gravity waves, *Can. J. Phys.*, *48*, 1458–1471, 1970.

Frisch, U., *Turbulence: The Legacy of A. N. Kolmogorov*, 296 pp., Cambridge Univ. Press, New York, 1995.

Gardner, C. S., Diffusive filtering theory of gravity wave spectra in the atmosphere, *J. Geophys. Res.*, *99*, 20,601–20,622, 1994.

Gardner, C. S., Testing theories of atmospheric gravity wave saturation and dissipation, *J. Atmos. Terr. Phys.*, *58*, 1575–1589, 1996.

Garrett, C., and W. Munk, Space-time scales of internal waves, *Geophys. Fluid Dyn.*, *2*, 225–264, 1972.

Garrett, C., and W. Munk, Space-time scales of internal waves: A progress report, *J. Geophys. Res.*, *80*, 291–297, 1975.

Gossard, E. E., and W. H. Hooke, *Waves in the Atmosphere*, 456 pp., Elsevier, New York, 1975.

Hamilton, K., Climatological statistics of stratospheric inertia-gravity waves deduced from historical rocketsonde wind and temperature data, *J. Geophys. Res.*, *96*, 20,831–20,839, 1991.

Harris, F. J., On the use of windows for harmonic analysis with the discrete Fourier transform, *Proc. IEEE*, *66*, 51–83, 1978.

Hass, H., and W. Meyer, Gravity wave fields above Andøya, *J. Atmos. Terr. Phys.*, *49*, 705–721, 1987.

Hines, C. O., Internal atmospheric gravity waves at ionospheric heights, *Can. J. Phys.*, *38*, 1441–1481, 1960.

Hines, C. O., The saturation of gravity waves in the middle atmosphere, II, Development of Doppler-spread theory, *J. Atmos. Sci.*, *48*, 1360–1379, 1991.

Hines, C. O., Pseudosaturation of gravity waves in the middle atmosphere: An interpretation of certain lidar observations, *J. Atmos. Terr. Phys.*, *55*, 441–445, 1993.

Hirota, I., and T. Niki, A statistical study of inertio-gravity waves in the middle atmosphere, *J. Meteorol. Soc. Jpn.*, *63*, 1055–1066, 1985.

Huang, N. E., Z. Shen, S. R. Long, M. C. Wu, E. H. Shih, Q. Zheng, N-C. Yen, C. C. Tung, and H. H. Liu, The empirical mode decomposition and the Hilbert spectrum for nonlinear and nonstationary time series analysis, *Proc. R. Soc. London A.*, in press, 1997.

Kaiser, G., *A Friendly Guide to Wavelets*, 300 pp., Birkhauser, Boston, Mass., 1994.

Karl, J. H., *An Introduction to Digital Signal Processing*, 341 pp., Academic, San Diego, Calif., 1989.

Landau, L. D., and E. M. Lifshitz, *Course of Theoretical Physics*, vol. 6, *Fluid Mechanics*, 2nd ed., 539 pp., Pergamon, Tarrytown, N. Y., 1987.

Lighthill, M. J., *Waves in Fluid*, 504 pp., Cambridge Univ. Press, New York, 1978.

Lindzen, R. S., Gravity waves in the mesosphere, in *Dynamics of the*

Middle Atmosphere, edited by J. R. Holton and T. Matsuno, pp. 3–18, Terrapub, Tokyo, 1984.

Marks, C. J., and S. D. Eckermann, A three-dimensional nonhydrostatic ray-tracing model for gravity waves: Formulation and preliminary results for the middle atmosphere, *J. Atmos. Sci.*, *52*, 1959–1984, 1995.

Miller, A. J., Response characteristics of meteorological rocket wind reduction techniques, *J. Geophys. Res.*, *74*, 6853–6858, 1969.

Offermann, D., The DYANA campaign: Survey, *J. Atmos. Terr. Phys.*, *56*, 1639–1657, 1994.

Panchev, S., *Random Functions and Turbulence*, 444 pp., Pergamon, Tarrytown, New York, 1971.

Press, W. H., S. A. Teukolsky, W. T. Vetterling, and B. P. Flannery, *Numerical Recipes in Fortran: The Arts of Scientific Computing*, 2nd ed., 963 pp., Cambridge Univ. Press, New York, 1992.

Sato, K., and M. Yamada, Vertical structure of atmospheric gravity waves revealed by the wavelet analysis, *J. Geophys. Res.*, *99*, 20,623–20,631, 1994.

Schmidlin, F. J., H. S. Lee, and W. Michel, The inflatable sphere: A technique for the measurement of middle atmosphere temperatures, *J. Geophys. Res.*, *96*, 22,673–22,682, 1991.

Senft, D. C., and C. S. Gardner, Seasonal variability of gravity wave activity and spectra in the mesopause region at Urbana, *J. Geophys. Res.*, *96*, 17,229–17,264, 1991.

Shimomai, T., M. D. Yamanaka, and S. Fukao, Application of wavelet analysis to wind disturbance observed with MST radar techniques, *J. Atmos. Terr. Phys.*, *58*, 683–696, 1996.

Smith, S. A., D. C. Fritts, and T. E. VanZandt, Evidence for a saturated spectrum of atmospheric gravity waves, *J. Atmos. Sci.*, *44*, 1404–1410, 1987.

Tsuda, T., T. Inoue, D. C. Fritts, T. E. VanZandt, S. Kato, T. Sato, and S. Fukao, MST radar observations of a saturated gravity wave spectrum, *J. Atmos. Sci.*, *46*, 2440–2447, 1989.

Tsuda, T., Y. Murayama, T. Nakamura, R. A. Vincent, A. H. Manson, C. E. Meek, and R. L. Wilson, Variations of the gravity wave characteristics with height, season and latitude revealed by comparative observations, *J. Atmos. Terr. Phys.*, *56*, 555–568, 1994.

VanZandt, T. E., A universal spectrum of buoyancy waves in the atmosphere, *Geophys. Res. Lett.*, *9*, 575–578, 1982.

Vincent, R. A., Gravity wave motions in the mesosphere, *J. Atmos. Terr. Phys.*, *46*, 119–128, 1984.

Vincent, R. A., and D. C. Fritts, A climatology of gravity wave motions in the mesosphere region at Adelaide, Australia, *J. Atmos. Sci.*, *44*, 748–760, 1987.

Wait, J. R., *Wave Propagation Theory*, 348 pp., Pergamon, Tarrytown, N. Y., 1981.

Warner, C. D., and M. E. McIntyre, On the propagation and dissipation of gravity wave spectra through a realistic middle atmosphere, *J. Atmos. Sci.*, *53*, 3213–3235, 1996.

Weinstock, J., Saturated and unsaturated spectra of gravity waves and scale-dependent diffusion, *J. Atmos. Sci.*, *47*, 2211–2225, 1990.

Wu, Y. F., and H. U. Widdel, Observational evidence of a saturated gravity wave spectrum in the mesosphere, *J. Atmos. Terr. Phys.*, *51*, 991–996, 1989.

Wu, Y. F., and H. U. Widdel, Saturated gravity wave spectrum in the polar lower thermosphere observed by foil shaff during campaign "Sodium 88," *J. Atmos. Sci.*, *49*, 1781–1789, 1992.

Yamanaka, M. D., and S. Fukao, A simple model of gravity-wave momentum and energy fluxes transferred through the middle atmosphere to the upper atmosphere, *J. Atmos. Terr. Phys.*, *56*, 1375–1385, 1994.

Zhu, X., Inertio-gravity waves in the middle atmosphere, Ph.D. dissertation, 165 pp., Univ. of Washington, Seattle, 1987.

Zhu, X., A new theory of the saturated gravity wave spectrum for the middle atmosphere, *J. Atmos. Sci.*, *51*, 3615–3626, 1994.

Zhu, X., and J. R. Holton, Mean fields induced by local gravity-wave forcing in the middle atmosphere, *J. Atmos. Sci.*, *44*, 620–630, 1987.

M. Bittner, Department of Physics, University of Wuppertal, W-5600, Wuppertal 1, Germany. (e-mail: bittner@mailgate.urz.uni-wuppertal.de)

S. D. Eckermann, E. O. Hulburt Center for Space Research, Code 7641, Naval Research Laboratory, Washington, D. C., 20375. (e-mail: eckerman@ismap4.nrl.navy.mil)

I. Hirota, Department of Geophysics, Faculty of Science, Kyoto University, Kyoto 606, Japan. (e-mail: hirota@kugi.kyoto-u.ac.jp)

Z. Shen, Department of Earth and Planetary Sciences, Johns Hopkins University, Baltimore, MD 21218. (e-mail: shen@cco.caltech.edu)

J.-H. Yee and X. Zhu, Applied Physics Laboratory, Johns Hopkins University, Johns Hopkins Road, Laurel, MD 20723-6099. (e-mail: jeng-hwa_yee@jhuapl.edu; xzhu@grant.jhuapl.edu)